J. Fluid Mech. (1989), *vol.* 200, *pp.* 309–336
Printed in Great Britain

Investigation of an excited jet diffusion flame at elevated pressure

By ANTHONY W. STRAWA† AND BRIAN J. CANTWELL‡

†NASA Ames Research Center, Moffett Field, CA 94035, USA.

‡Department of Aeronautics and Astronautics, Stanford University, Stanford, CA 94305, USA.

(Received 13 November 1987 and in revised form 30 June 1988)

Experiments have been carried out with the objective of studying the relationship between flow structure, flow excitation and the reaction process in the near field of a low-speed coflowing jet diffusion flame. The effect of axial forcing and increasing pressure on the structure and controllability of the flame has been studied in an attempt to elucidate some of the underlying mechanisms of control. The experiments were conducted in a variable-pressure flow facility which permits the study of reacting flows at pressures ranging from 10 to 1000 kPa (0.1 to 10 atm.). The flame was excited by adding a small-amplitude, periodic fluctuation to the central fuel jet exit velocity. The flow was visualized using an optical scheme which superimposes the luminous image of the flame on its schlieren image, giving a useful picture of the relationship between the luminous soot-laden core flow and the edge of the surrounding hot-gas envelope. Phase-conditioned velocity measurements were made with a one-component laser Doppler anemometer. The excitation frequency was varied, and it was found that a narrow band of frequencies exists in which several of the instabilities of the flow seem to be in coincidence, causing the flame to break up periodically into a series of distinct eddies. Hereafter this will be called the strongly coupled state. Maps of the one-dimensional velocity vector field, viewed in a frame of reference convecting with the large eddies, are used to study the topology of the flow. When the excitation frequency lies above the strongly coupled range, the flow pattern is found to contain stagnation points which straddle the axis of the jet. When the excitation frequency is reduced to a point where strong coupling occurs the stagnation points move onto the axis promoting breakup of the flame. As the pressure is increased, the relative role of diffusion is decreased and the flame becomes highly three-dimensional. In the strongly coupled state, the flow continues to be very periodic, even to the extent that much of the three-dimensional structure is repeatable from cycle to cycle.

1. Introduction

Recent experiments in turbulent combustion have emphasized the interaction between flow structure and the reaction process. This interaction is an important part of most real combusting systems. Although our understanding of the physics of turbulent combustion has improved recently, there are as yet no data that directly reveal the relationship between the unsteady velocity field and the unsteady reaction field in a turbulent flame. A better understanding of this relationship is central to the development of improved models of combustion and to the development of methods for eventually controlling combustion.

The jet diffusion flame has been an object of interest since the time of Rayleigh's

early experiments in 1877 and has received renewed interest with the advent of advanced diagnostic techniques. Recent studies of high-Reynolds-number flames have been conducted by Chigier & Yule (1979), Yule *et al.* (1980), Roquemore *et al.* (1984), and Dibble, Kollman & Schefer (1984). These have concentrated on obtaining statistical properties of the velocity field and conserved scalars and on flow visualization using photography and schlieren methods. Rayleigh and others have noted regular flickering oscillations in diffusion flames. Chamberlin & Rose (1928) reported that the frequency of oscillations was about 10 Hz and was independent of fuel flow rate, jet diameter, and fuel composition for the gases they investigated. More recently Ballantyne & Bray (1977), Becker & Liang (1983), and Grant & Jones (1975) have noted that these instabilities can lead to the breakup of the flame in a quasi-periodic fashion at frequencies between 5 and 15 Hz.

In the present study we have investigated the near field of a low-speed coaxial jet diffusion flame at low to moderate Reynolds and Grashof numbers. We chose to excite the flame in a range near its natural flickering frequency to produce a periodic flow suitable for conditional sampling. It was found that by using a loudspeaker to apply a small-velocity perturbation to the central fuel jet, an extremely periodic flow could be produced. Moreover, by changing the frequency of excitation, it was found that the structure of the flow field could be controlled, thus influencing the reaction and mixing processes. The idea of exciting natural instabilities to obtain a periodic flow has been used effectively by others to study the large eddies in cold flows. See, for example, Perry & Lim (1978) and Lepicovsky (1986). Very recently this approach was used by Lewis *et al.* (1988) in a study of a flickering laminar diffusion flame at one atmosphere.

The main goal of the work was to document the relationship between flow structure, flow excitation, and the reaction process by using phase-conditioned velocity measurements to obtain a map of the unsteady flow field which is compared to flow visualization photographs. A topological approach is used in an attempt to describe changes in the structure of the flame. This has been applied successfully to cold flows (see the recent review by Perry & Chong 1987) and is presently being utilized by Lewis *et al.* (1988) but we are unaware of any previous application to a flame. The phase-conditioned velocity measurements are used to construct maps of the instantaneous, unsteady velocity field. When the field is observed from a frame of reference moving with the large-scale eddies, a topological pattern can be inferred and described using critical-point terminology. This provides a systematic means of classifying structural features of the flow and may eventually have useful applications in relating large-eddy motions to entrainment and mixing processes in unsteady flames.

2. The variable-pressure flow facility

The experiments were conducted in a new flow facility which was designed to allow the study of reacting and non-reacting flows over a wide range of flow conditions using a variety of optical techniques. The facility has a variable pressure capability that allows the flow Reynolds number to be changed without changing flow timescales. Optical acess is achieved through four large, high-temperature schlieren-quality glass windows mounted on all four sides of the test section. The facility can be closed to the atmosphere, allowing the use of exotic gases and seed materials. A modular design was used which allows rapid and inexpensive modification of the facility configuration.

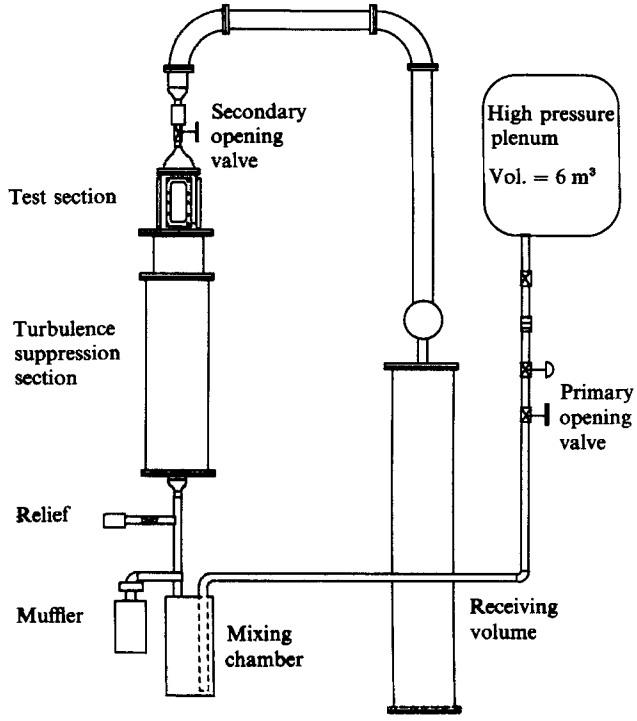

FIGURE 1. Schematic showing flow facility.

Figure 1 shows a layout of the facility. The flow originates in a 6 m^3 spherical pressure vessel at a maximum pressure of 18600 kPa. The flow is filtered and the pressure is regulated down to several thousand kPa by a Grove balanced valve dome regulator. Next, after passing through a choked 5.08 cm Masoneilan upstream control valve, the flow passes through a mixing chamber that houses a TSI atomizer which is used to speed the flow for the laser Doppler anemometer (LDA). The mixing chamber is well upstream of the test section to ensure a homogeneous seed-particle distribution in the free stream. After the mixing chamber, the flow passes first through a 48.26 cm diameter turbulence suppression section containing a series of screens and perforated plates, and then through a 3:1 axisymmetric contraction and a 1.5:1 circular to rectangular contraction prior to entering the test section. The test section is 10 by 15 cm in cross-section and 40 cm in length and is constructed from nickel-plated steel (figure 2). Note that the inside walls of the test section are located 2.54 cm to either side of the edges of the optical viewing area defined by the rather massive window frames seen in figure 2 and the flow is not significantly blocked (as it may appear in the flow visualization photographs). The flow then exits the test section to a sudden-area-change expansion followed by a contraction to a second Masoneilan control valve identical to the upstream valve, but with a larger orifice. Together, the upstream and downstream valves permit the velocity and pressure in the test section to be varied independently. The spent gases may be exhausted to the atmosphere or trapped in four large stainless steel receiving volumes for later processing and disposal. The exposed inside surfaces of the facility are coated with a cured, acrylic, high-temperature epoxy paint for corrosion protection from exotic gases.

The facility has a velocity range of 0.5 to 10 m/s and a pressure range of

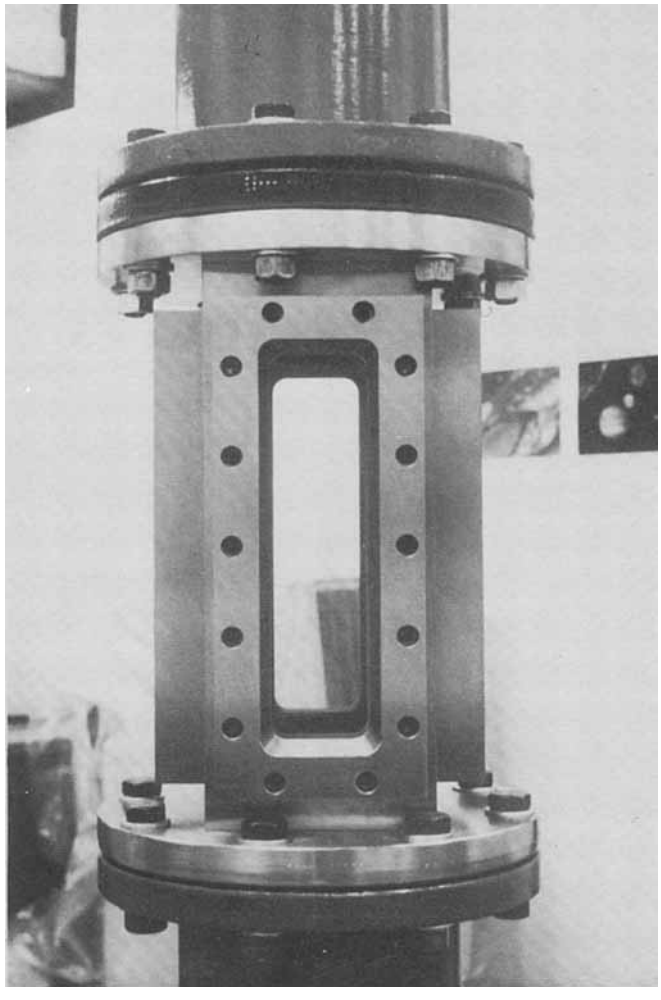

FIGURE 2. Test section.

10–1000 kPa, giving an effective Reynolds number range of 5×10^2–10^6 cm^{-1} with a maximum air mass flow rate of 1.84 kg/s. The tunnel can be run for long periods when exhausting into the atmosphere. For test-section pressures below atmospheric pressure, or when exotic gases or seeding are used, run times are limited to about 10–20 s by the size of the receiving volumes. Turbulence intensities in the facility at the low velocities used in this experiment were measured at about 0.5–1%. Repeatability of free-stream velocity is estimated at 1% of free stream over the operating range of the facility.

3. Overview of the experiment

Figure 3 shows the experimental configuration. The air stream enters the test section at velocity U_{FS}. Bottled methane gas is regulated, split into two streams, and passed through two rotameters. One fuel stream goes directly to the fuel plenum

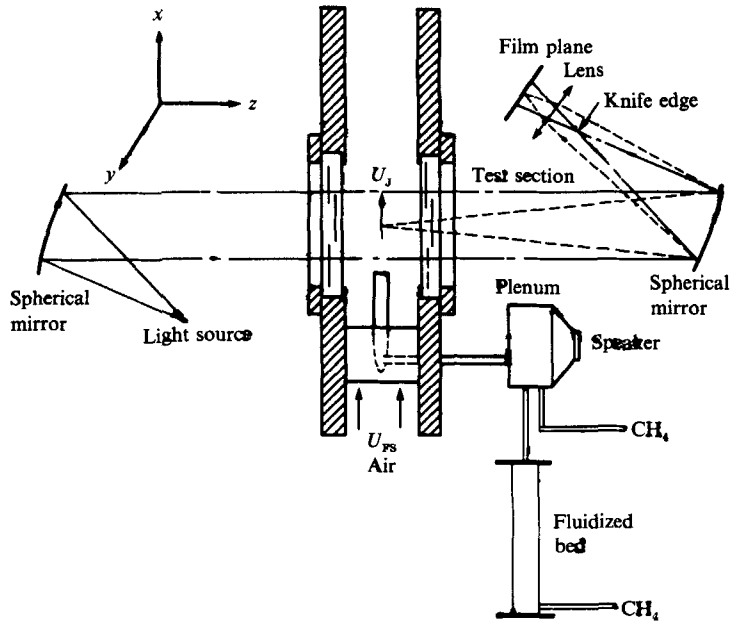

FIGURE 3. Schematic of the schlieren system. Solid lines trace the light rays that formed the schlieren image, and dashed lines trace the light rays that formed the image of the luminous sooting region of the flame. The jet exit diameter is 2.2 cm and the test-section dimensions are 10.2 by 15.2 cm.

while the other passes through a fluidized bed that seeds the fuel with Al_2O_3 particles prior to entering the plenum. The plenum houses a loudspeaker that is used as a fluctuating volume source to add a small perturbation to the fuel-jet exit velocity. The fuel gas then flows into the main air-stream near the entrance to the test section at a mean jet exit velocity U_J. The jet is 2.2 cm in diameter and is supported by a streamlined strut which spans the 10 cm width of the test section. Figure 3 also shows the coordinate system used in the experiment. The streamwise direction is labelled as the x-axis with gravity acting in the minus x-direction. The schlieren optical axis is the z-axis and the LDA was transversed along the z-axis, referred to as the spanwise direction. The coordinate system origin was at the centre of the jet exit.

The experimental variables were: the cold jet exit velocity, U_J; the free-stream velocity at the jet exit, U_{FS}; the acoustical excitation frequency, f; and the test-section pressure, P_{TS}. The free-stream and cold jet velocities were varied only to achieve the most stable and periodic flow for the chosen pressure and excitation frequency. Once the flow was established, the velocities were held fixed. Nine cases were investigated with combinations of three pressures and three excitation frequencies. These are listed in table 1. The test-section pressures were, nominally, 101, 239, and 446 kPa (nominally 1, 2 and 4 atm.). Three frequencies are listed for each pressure, corresponding to the natural flickering frequency of the flame, the excitation frequency that corresponded to strong coupling, and an excitation frequency at about twice the natural frequency. The experiments cover a Reynolds-number range from 700 to 2600 based on cold jet exit conditions.

In considering the possible interplay between instability modes in the flame and

Case no.	P_{TS} kPa	Freq. Hz	U_J m/s	U_{FS} m/s	U_{PH} m/s	H cm	α degrees	Re	Ri
1	101	10*	0.48	0.48	—	61	—	728	4.9
2	101	10	0.48	0.48	0.61	51	10	728	4.9
3	101	20	0.48	0.48	—	61	7	728	4.9
4	239	9.8*	0.17	0.40	—	33	—	600	39
5	239	9.8	0.17	0.40	0.69	25	10	600	39
6	239	17	0.17	0.40	—	30	8	600	39
7	446	9.6*	0.40	0.36	—	33	—	2640	7.0
8	446	9.6	0.40	0.36	0.72	20	10	2640	7.0
9	446	20	0.40	0.36	—	28	7	2640	7.0

TABLE 1. Case numbers, initial conditions, and observed flame characteristics from visual data. The unforced natural frequency is indicated by an asterisk.

the acoustics of the facility, it was observed that the test section had a resonance of 20–25 Hz when it was open to the atmosphere (as in the 101 kPa case), and a resonance of 55–60 Hz when closed to the atmosphere (as in the 239 and 446 kPa cases). In addition, a resonant peak at 9 Hz was observed in the frequency response of the speaker/plenum system. This raised a concern as to whether the facility-plenum acoustics might be determining the natural frequency of the flame or triggering the strong coupling condition.

Another area of concern related to the geometry of the jet tube. The tube is rather short, and with the small jet diameter and the low velocities used in these experiments, it was quite difficult to control the profile shape, which tended to be only partially developed, with a flat region near the centreline and a thick, viscous layer near the wall. The initial flow is affected by the presence of a relatively thick jet lip of about 3 mm, which was required to hold a stable flame. In some preliminary experiments we found the flame blow-off speed to be extremely sensitive to the presence of coflow, with the flame tending to blow off when the coflow speed exceeded the laminar flame speed. In order to operate at a reasonable coflow velocity a thick jet lip was required with its associated wake complicating the jet initial conditions. However, the wake deficit diffuses rapidly and does not appear in the velocity measurements at the downstream measuring station.

Hot-wire measurements of the axial velocity were taken near the jet exit to confirm that the fluctuation was reasonably sinusoidal and apparently free of harmonic distortion over the range of excitation frequencies. The perturbation in the jet exit velocity, at an excitation of 9 Hz, was measured at 5–10% of the mean jet velocity when the amplifier output voltage was 5 V peak to peak. The flow structure did not appear to change with moderate increases in speaker amplitude.

Both of the above issues were studied in a 101 kPa (1 atm.), open-return flame visualization tunnel constructed with nearly the same test-section geometry as the pressurized rig, but with a slightly smaller jet tube which was fed from a plenum with a smooth contraction and about 20 diameters of entry length. This rig is described in more detail in Lewis, Cantwell & Lecuona (1987). Under similar Reynolds-number and Richardson-number conditions, the flame observed in this rig was visually identical to the flame studied in more detail in the variable-pressure rig. Preliminary experiments showed a flame with frequency and coupling characteristics which were very similar to the flame observed in the variable-pressure rig, even though the

Case no.	Freq. Hz	Seed	$\overline{U_{cl}}$ m/s	U_{rms} m/s	a m/s^2
7A	9.6*	H_2O	0.78	0.38	4.2
7B	9.6*	Al_2O_3	1.54	0.68	17.1
7C	9.6*	both	1.36	0.67	13.7
8A	9.6	H_2O	0.88	0.29	4.2
8B	9.6	Al_2O_3	0.96	0.22	5.4
8C	9.6	both	0.86	0.31	4.1
9A	20	H_2O	1.64	0.31	19.7
9B	20	Al_2O_3	1.95	0.62	28.6

TABLE 2. Case numbers and computed centreline velocites for the 446 kPa LDA data. The measurements were taken 3 diameters from the jet exit. The unforced natural frequency is indicated by an asterisk.

acoustic characteristics of the 1 atm. rig are quite different. Moreover, the behaviour of the flame was found to be independent of the amplitude of the excitation once the amplitude was sufficient to cause the flow to lock onto the excitation. This corresponded to an excitation level of several percent of the jet velocity. As mentioned previously, the characteristic 10 Hz natural frequency of diffusion flames has been observed by a number of other investigators and is not unique to our facility or experimental set-up.

It appears that under low-speed combusting conditions, dominated by buoyancy, the flow becomes essentially independent of the jet exit flow within a very few diameters, except to the extent that the fuel volume flow rate determines the overall heat release rate. The discussion in this paper is restricted to those aspects of flame behaviour that are likely to be common to all flames of similar geometry. This includes a kinematic and topological discussion of flame breakup, and a comparative description of the effects of different forcing frequencies on the velocity field and visual flame structure in regions of the flow field which are away from the jet exit.

Table 2 lists the flow conditions for the 446 kPa velocity measurements. All measurements were made 3 jet diameters from the jet exit. Three types of seeding were used in acquiring the velocity data. Data were taken with only the outer free-stream flow seeded with water droplets to mark the free-stream air fluid. Data were also taken with only the inner gas flow seeded with Al_2O_3 particles to mark the jet fluid. Finally, data were taken with both fluids seeded simultaneously for comparison. The case numbers are modified by the letters A, B, and C to indicate respectively that the flow was seeded with water droplets, with aluminum oxide particles, or with both seedings.

4. Instrumentation and data reduction

Figure 3 depicts the optical arrangement used for the flow visualization. Light from a continuous mercury-arc source is collimated, passed through the test section, focused onto a knife edge and then imaged on the film plane of a camera. Light originating from the flame is also focused onto the image plane. The result is a colour picture which combines the schlieren effect with the image of the luminous portions of the flame. Movies were made using a Photosonics high-speed camera with 16 mm

Kodak VNX 7399 film at 400 frames/s. Figures 5–7 show sequences taken from these movies. Figures 15 and 16 show still photographs taken with a Canon FTb camera using Kodacolor VR ASA 400, 35 mm colour film at a shutter speed of 1/500 s.

The large index-of-refraction variations associated with large temperature gradients which occur in the flame raised some question as to the accuracy to which boundaries of the hot-gas envelope can be determined from the schlieren pictures. Both ray-tracing and statistical methods were used for estimating the maximum error and are discussed in Strawa (1986). In the worst case the uncertainty in the position of the boundary is approximately 0.01 jet diameter.

The laser Doppler anemometer system used to make the velocity measurements employed the 514.5 nm line of an Ar^+ laser with a forward-scatter, differential-Doppler technique. Figure 4 shows the LDA and data-acquisition system layout. The focal volume size was approximately 0.5×1.0 mm. The LDA system was calibrated against a spinning disk and it was found that the actual velocities were 1.2% higher than measured by the LDA. This is well within the error due to thermophoretic effects and sampling bias, discussed below, which we estimate to be on the order of 5–7% (indicated in the form of an error bar in figure 8). The analogue LDA signal was fed into a TSI Model 1980 processor interfaced with a DEC MINC-11/03 lab computer. In order to conditionally sample the velocity data collected with the LDA system, phase information was needed relative to the sine wave forcing the flame. The function generator produced a sync pulse at the positive zero-crossing of the sine wave. The sync pulse caused the computer's programmable clock to start counting. Each time the processor sent a valid data point to the computer, the clock was queried for a count. Using this information and the known period of the function generator, a phase could subsequently be determined. The raw velocity and phase data were transferred to memory via a direct-memory-access interface. The raw data were later transferred onto diskettes for storage. The data-acquisition process is explained fully in Strawa (1986).

Two types of particles were used to seed the flow for the LDA system. The outer flow was seeded with water droplets using a TSI six-jet atomizer housed in the mixing chamber shown in figure 1. Based on the nominal droplet sizes generated by this atomizer we estimate that the time for a water droplet to evaporate when it comes into contact with the high temperatures of the reaction zone is about 10 μs. The fuel-jet fluid was seeded by passing it through a fluidized bed filled with Al_2O_3 particles. Both types of particles had diameters distributed between 1 and 5 microns.

Flames present significant difficulties with respect to obtaining a homogeneous distribution of seed particles. The inhomogeneities in seed density which may not be apparent in an ordinary average of the flow are clearly brought out in the ensemble average. This stems from heterogeneous mixing in the two streams, flow dilation and thermophoresis. Thermophoresis as described by Friedlander (1977) is the transport of particles in a temperature gradient, from high to low temperatures, due to Brownian motion. In a separate study of this effect, Lewis *et al.* (1987) estimated the thermophoretic velocity for particles of the size needed for LDA measurements in this flame to be between 1 and 3 cm/s in a direction away from the maximum temperature region of the reaction zone. The combined effects of mixing, flow dilation, and thermophoresis cause data rates within some regions of the flame to be very low, in some cases dropping below one sample per second.

All of the velocity data presented here are for the 446 kPa case at a streamwise location of 3 jet diameters above the jet exit. Overall average and root-mean-squared

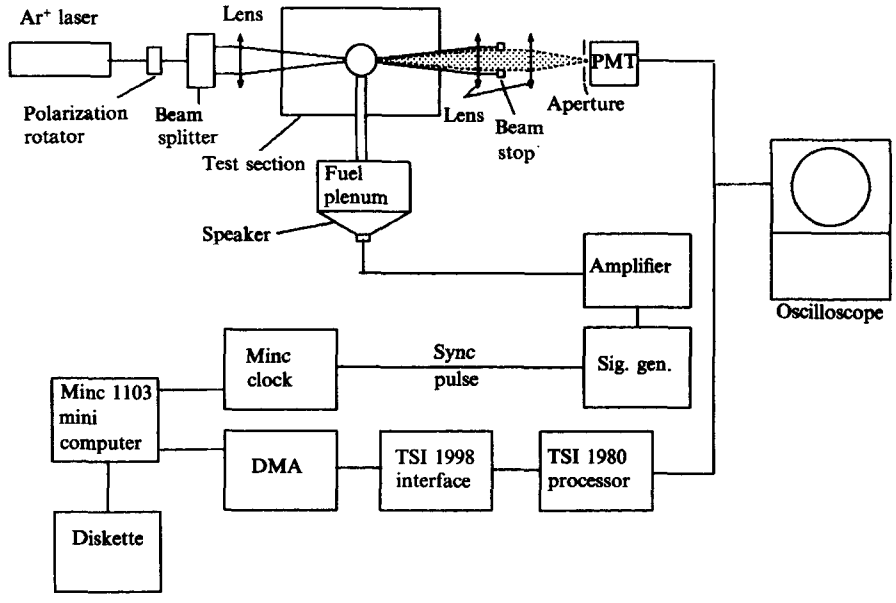

FIGURE 4. Schematic of the LDA and phase data-collection system. Data from the LDA are processed by TSI electronics and sent to a microcomputer. Phase information is collected by the computer for each valid velocity data point.

(r.m.s.) velocities were measured at several spanwise locations. The average velocity was corrected for velocity-related sampling bias errors by the formula

$$\langle u \rangle = \frac{\sum_{n=1}^{N} u_n \Delta t_n}{\sum_{n=1}^{N} \Delta t_n}, \tag{1}$$

where N is the total number of measurements collected at this location, u_n is a velocity sample, and Δt_n is the time of flight for the nth sample. Root-mean-square velocity fluctuations were determined from

$$u_{\text{rms}} = \left(\frac{1}{N} \sum_{n=1}^{N} (u_n - \langle u \rangle)^2 \right)^{\frac{1}{2}}. \tag{2}$$

The N samples were also sorted into 30 phase bins, and bin-average and r.m.s. velocities were calculated in a similar fashion.

Although the above scheme corrects for velocity-related sampling bias errors it does not correct for density-related sampling bias errors and no scheme that we are aware of can do this short of simultaneously measuring velocity and density. Sorting the data according to phase removes the bias errors due to fluctuations associated with the periodic part of the motion but errors due to fluctuations at a given phase remain. A further source of bias errors arises when both streams are seeded simultaneously. If the seeding densities are not exactly matched then mixing-related sampling errors will occur owing to the higher probability of measuring the more

densely seeded fluid. For this reason we present data for which one or the other of the two streams is seeded but not for the case where both streams are seeded.

The one-dimensional velocity measurements are useful in that they compliment the visualization results and without them we could reach few conclusions concerning many aspects of the basic flow structure especially within the flame. For reasons of low data rate and sampling bias we decided not to carry out a more extensive study of the velocity field. We feel that to accomplish this an alternative approach to laser anemometry will be required. Lewis *et al.* (1987) report the development of a particle tracking technique for velocity measurement in flames based on the use of a copper-vapour laser and aluminum oxide particle seeding. Particle track measurements of the unsteady velocity field in a low-Reynolds-number flame with both inner and outer flow seeded have been carried out by Lewis *et al.* (1988) and the initial results are encouraging. The technique has the great advantage of providing nearly instantaneous vector data over a field. It is biased in the sense that only velocity vectors that lie in the plane of the laser sheet are measured. For this reason the technique is not particularly useful for developing statistical information about the flow. Moreover, the spatial resolution is limited by the density of seeding which is subject to the effects of thermophoresis and volume change discussed above. In spite of the limitations just discussed, particle tracking appears to us at this time to be the most promising particle-based method for measuring flame velocity fields.

5. Basic parameters and scales

To aid in the comparison of the velocity measurements and visual observations, it was helpful to keep length and time scales of the flow the same while varying the Reynolds and Grashof numbers. This was accomplished by varying the test-section pressure. In a low-speed flame the buoyancy caused by the density change in the hot part of the flame is a significant factor in determining the dynamics of the flow. In order to define a consistent set of dimensionless parameters it is necessary to adopt a convention regarding the choice of gas properties. We shall use the convention that all gas properties are referred to the properties of the cold fuel at the jet exit. However, in describing the effects of buoyancy, it is necessary to use an effective gravitational acceleration defined as

$$g' = \left(\frac{\rho_{\mathrm{FS}} - \rho_{\mathrm{H}}}{\rho_{\mathrm{H}}}\right) g, \tag{3}$$

where ρ_{FS} is the density of the free-stream air and ρ_{H} is the density of the hot combustion gases. Since we have no direct measurements of temperature in these experiments, and since the temperature varies widely throughout the flame, it is necessary to pick a nominal value of ρ_{H} to characterize the flame. Here we have chosen a hot combustion gas temperature of 1600 K based on experimental evidence in typical diffusion flames. This temperature is used along with the test-section pressure to compute ρ_{H}.

There are two important timescales in the near field of a low-speed buoyant jet. The first is an inertial time proportional to the time it would take the jet fluid to convect one jet diameter,

$$\tau_1 = \frac{d}{U_{\mathrm{J}}}. \tag{4}$$

Other inertial timescales can be formed from the various parameters of the experiment; however for the sake of convention we shall use τ_1 as the appropriate normalizing quantity. The second timescale is proportional to the time it would take the jet fluid to convect one jet diameter under the acceleration of gravity,

$$\tau_2 = \left(\frac{d}{g'}\right)^{\frac{1}{2}}. \tag{5}$$

The Richardson number may be defined as the ratio of the square of these two times,

$$Ri = \left(\frac{\tau_1}{\tau_2}\right)^2, \tag{6}$$

and is a measure of the relative importance of buoyancy and inertia forces. The Richardson number is related to the Reynolds and Grashof numbers by

$$Ri = \frac{Gr}{Re^2}. \tag{7}$$

The Reynolds number is defined as

$$Re = \left(\frac{p}{RT_J}\right)\frac{u_J d}{\mu_J}, \tag{8}$$

and the Grashof number is

$$Gr = g'\left(\frac{d^3}{\mu_J^2}\right)\frac{p^2}{(RT_J)^2}. \tag{9}$$

The significance of this discussion with respect to our experiments is that for a given jet diameter and fuel, the Reynolds number is proportional to the product of jet velocity and test-section pressure. Whereas the Richardson number is inversely proportional to the jet velocity squared and independent of the test-section pressure.

Buoyancy forces dominate in flows where $Ri \geqslant 1$. The Richardson number in this experiment was always greater than four. Other non-dimensional numbers are also used by some authors to characterize reacting flows. For example, Roper (1977) uses a modified Froude number to relate momentum to buoyancy forces. He defines this as

$$Fr = \frac{v_{fo}^2}{aH}, \tag{10}$$

where v_{fo} represents a balance between the momentum of the combustion products in the reaction zone and the fuel and air from which they were formed. The quantity a is the mean upward acceleration of the flame due to buoyancy and H is the diffusion flame height. According to Roper's criterion, buoyancy dominates the flame when the value of the modified Froude number is much less than one. When these parameters are evaluated for the flame in this experiment, a value of $Fr = 0.04$ is obtained.

The natural frequency of the flame can be normalized using either the inertial time, τ_1 or the buoyancy time, τ_2. When the natural flickering frequency is combined with the inertial timescale in the 101 and 446 kPa cases a Strouhal number of 0.4 is obtained. The correspondence between this value and the Strouhal number of a non-buoyant jet is essentially fortuitous and, in fact, the flickering frequency and overall flame structure is practically independent of the jet exit velocity. See, for example, Chamberlin & Rose (1928), and Ballantyne & Bray (1977). This can be seen by

looking at the 230 kPa case where the Strouhal number based on the inertial time was close to one. This suggests that the appropriate non-dimensionalizing parameter should be the buoyancy timescale. However, attempts to correlate the flickering frequencies of low-speed flames in this fashion have not met with much success (Becker & Liang 1983). To investigate this issue further Subbarao (1987) carried out an experimental investigation of the effect of Reynolds number and Richardson number on the structure of a coflowing jet of helium in air. The density ratio of helium to air is comparable with the density ratio of hot products to air in the near field of a methane–air flame. The basic idea in this work was to remove the complicating effects associated with the spatial and temporal distribution of buoyancy forces in the near field of the jet. It was found that for a Richardson number larger than one the natural frequency of the helium jet correlated extremely well with the buoyancy timescale. With forcing, the helium jet did not exhibit the variety of modes exhibited by flames and typified here by the strong and weak coupling cases. The presence of buoyancy produces a flow with an overall structure that resembles the flame, but the absence of the flame sheet produces a flow that is very insensitive to perturbations of the jet exit velocity.

These results suggest that the physical explanation of strong coupling lies in the complex interplay between the jet exit velocity field, the position of the flame sheet and the stability of the axisymmetric plume which rises from the point of ignition. The effect of forcing is to modify the relationship between these three quantities affecting the distribution of buoyancy, thus affecting the downstream development of the flow. The flame-induced plume, absent in the cold flow case, has a characteristic width that is essentially independent of jet diameter. This adds a lengthscale to the problem complicating the diameter dependence of the natural flickering frequency. Issues of controllability, flame holding and flame flickering as well as soot formation all revolve about the nature of the flow in the very near field of the jet.

Owing to the complexities involved in choosing an appropriate timescale and because of the insensitivity of the flame to the mean jet exit velocity we have chosen to present our measurements in dimensioned form. Since velocity measurements for only one pressure case with uniquely specified jet exit and free-stream velocities are presented here this should not be a source of confusion and will serve as a reminder of the low-speed nature of the flow.

6. Results and discussion

6.1. *Visual observations*

Sixteen-mm motion pictures were made of the flame at a rate of 400 frames/s. In these movies, the flame is superimposed on its schlieren image at each of three pressures: 101, 239, and 446 kPa. Figures 5–7 (plates 1–3) are sequences of frames taken from the movies. Note that the test-section walls extend 2.5 cm on either side of the optical viewing area. The flame was excited by adding a periodic fluctuation to the central fuel-jet exit velocity. Jet exit velocities were measured with a constant-temperature hot wire and the signal was found to be sinusoidal with the perturbation in the jet exit velocity, at an excitation of 9 Hz, measured to be 5–10 % of the mean jet velocity. The flow structure did not appear to change with moderate increases in the amplitude of the perturbation. By forcing the jet in a range of frequencies encompassing its unforced natural frequency, it was possible to produce a very periodic and controllable flow. In the unforced flow, and over most of the driving

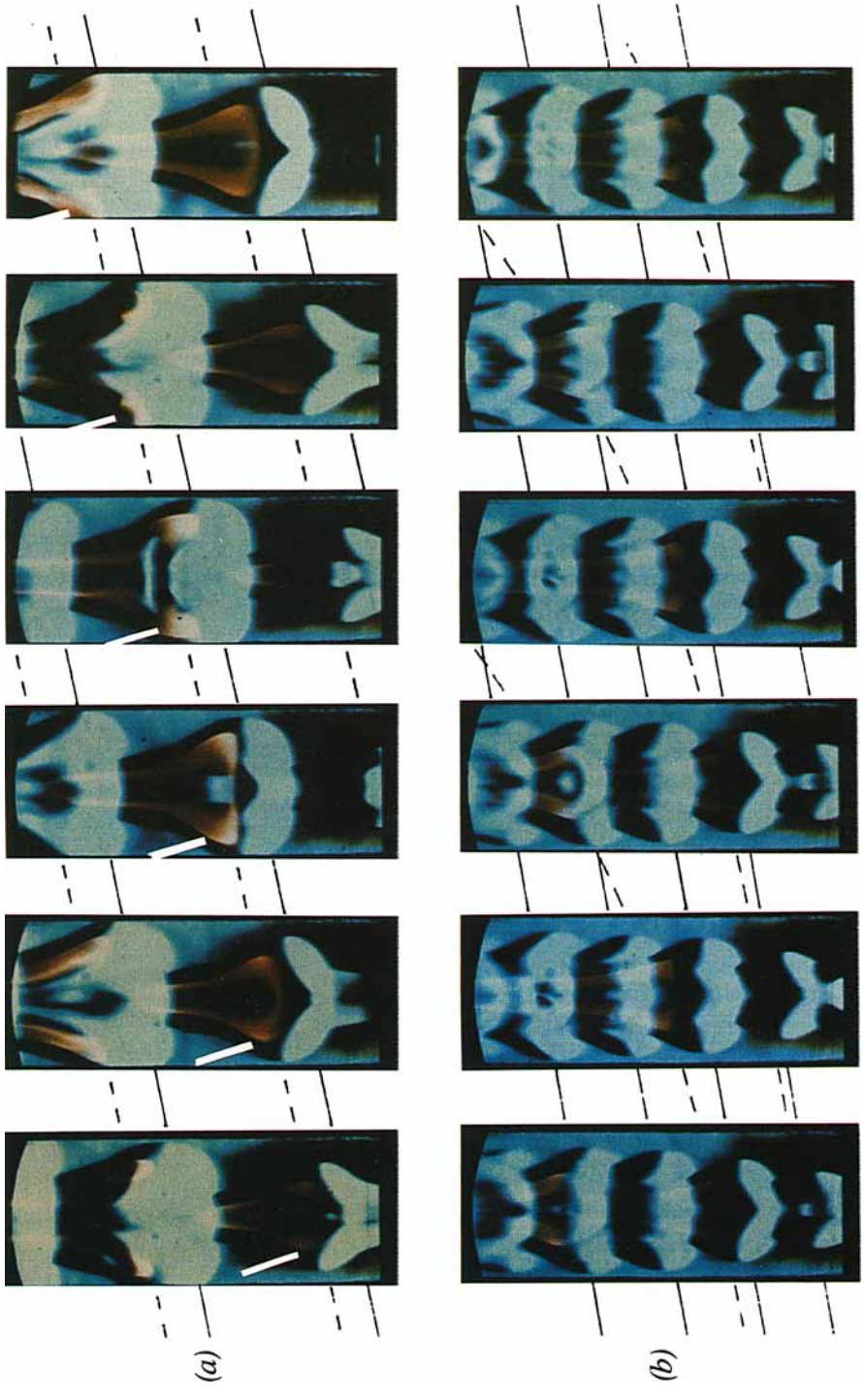

FIGURE 5. Sequence of pictures from a high-speed movie showing the evolution of a forced coflowing diffusion flame. The test-section pressure is 101 kPa. U_J and U_{FS} are 0.48 m/s. In *(a)* the jet is forced at 10 Hz and in *(b)* at 20 Hz. Time between frames is 0.04 s. The solid lines trace the trajectory of a bulge in the outer hot-gas envelope. The broken lines trace the trajectory of the luminous soot-laden core gas. (Reprinted by permission of *The Physics of Fluids* from Strawa & Cantwell 1985.)

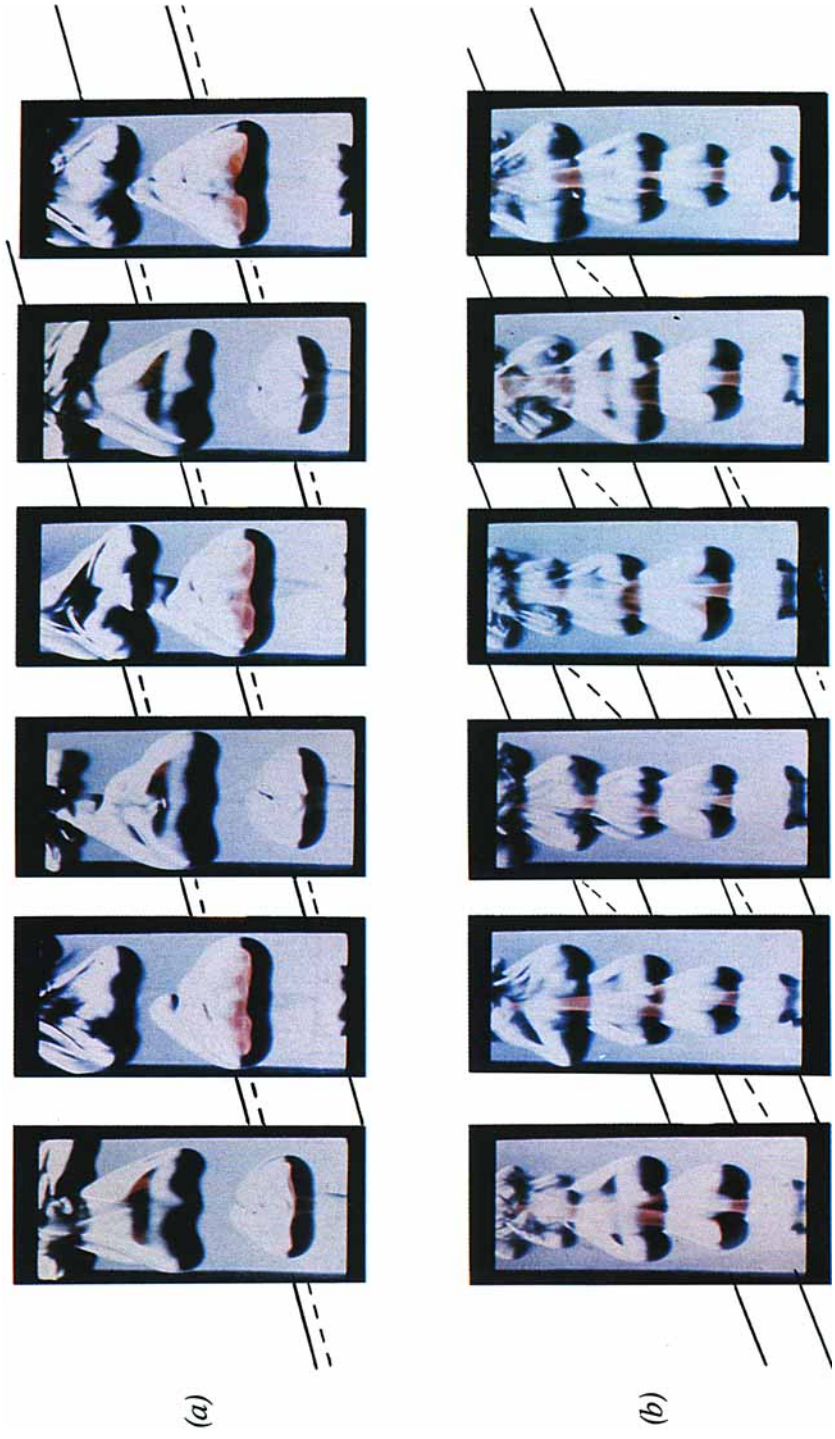

FIGURE 6. Sequence of pictures from a high-speed movie showing the evolution of a forced coflowing diffusion flame at 239 kPa. U_J is 0.17 m/s and U_{FS} is 0.4 m/s. In *(a)* the jet is forced at 9.8 Hz and in *(b)* at 17 Hz. Time between frames is 0.04 s. The solid lines trace the trajectory of a bulge in the outer hot-gas envelope. The broken lines trace the trajectory of the luminous soot-laden core gas.

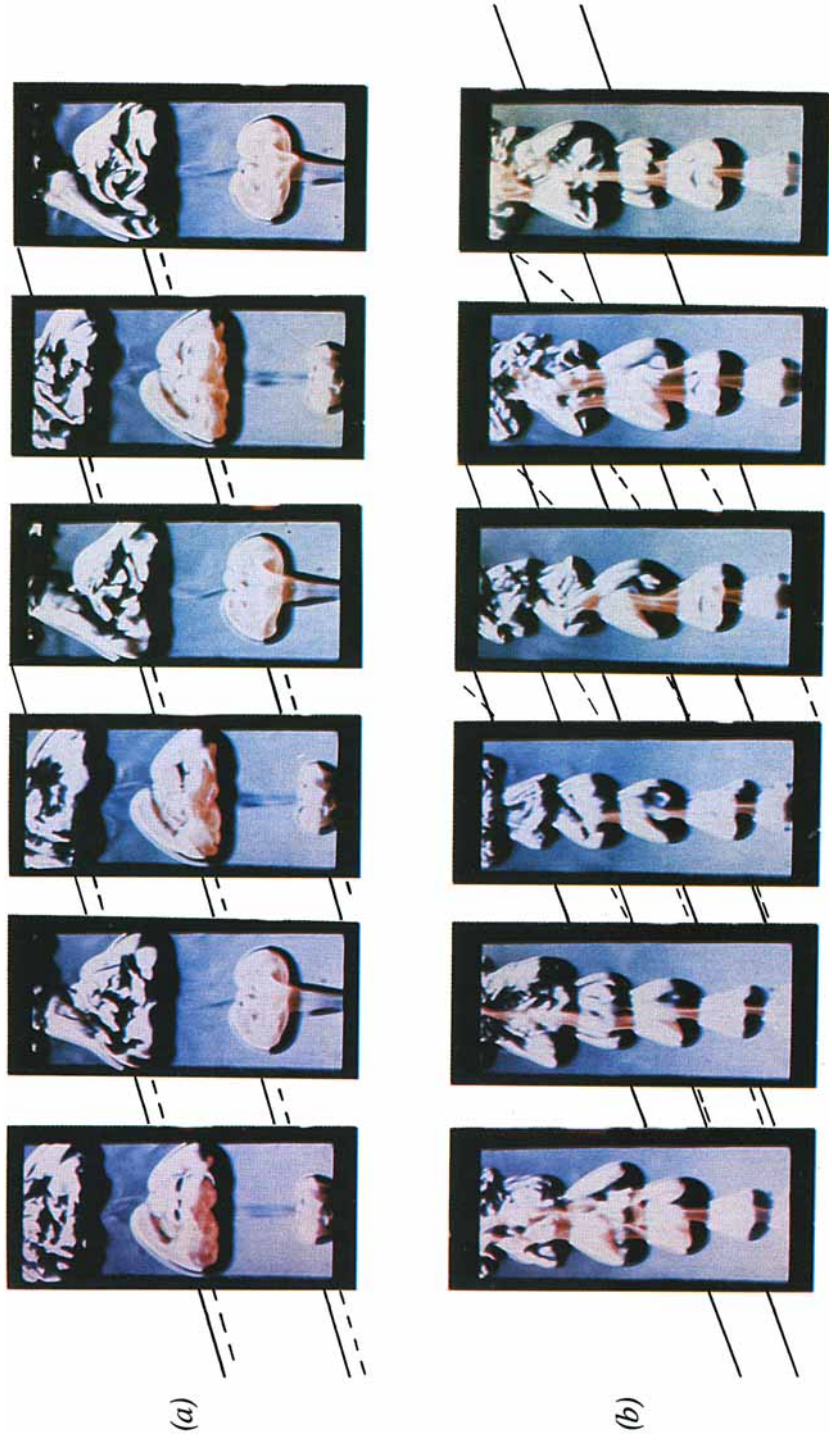

FIGURE 7. Sequence of pictures from a high-speed movie showing the evolution of a forced coflowing diffusion flame at 446 kPa. U_J is 0.40 m/s and U_{FS} is 0.36 m/s. In *(a)* the jet is forced at 9.6 Hz and in *(b)* at 20 Hz. Time between frames is 0.04 s. The solid lines trace the trajectory of a bulge in the outer hot-gas envelope. The broken lines trace the trajectory of the luminous soot-laden core gas.

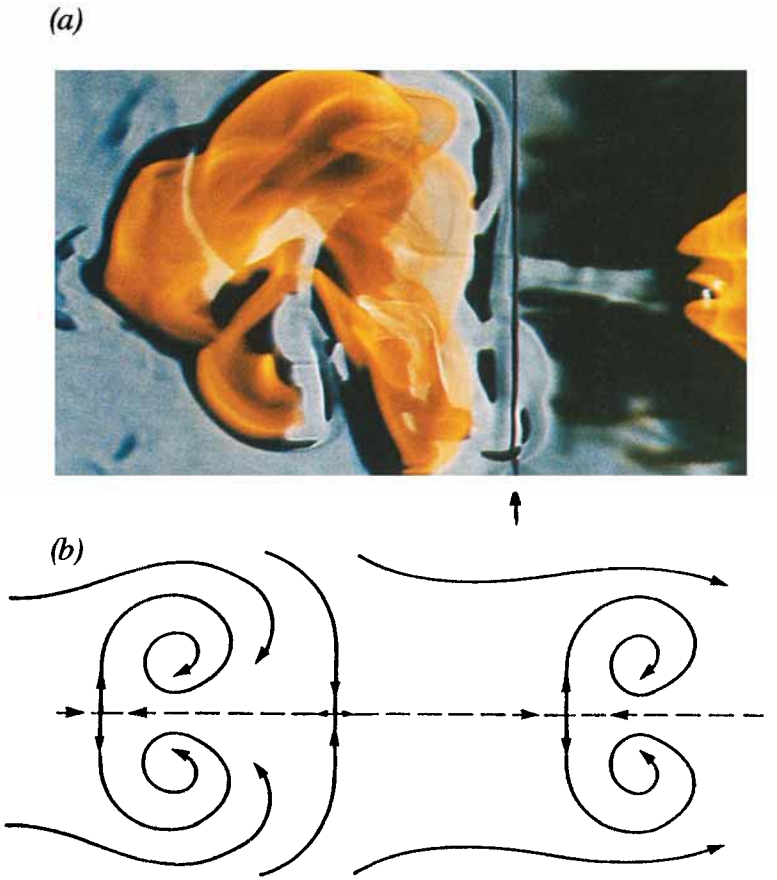

FIGURE 15. Comparison of conjectured velocity field of the strongly coupled case with a photograph of the flame. The arrow indicates where the velocity measurements were made. *(a)* Photo with the jet exit at the right. *(b)* Conjectured vector field with a celerity of 0.72 m/s.

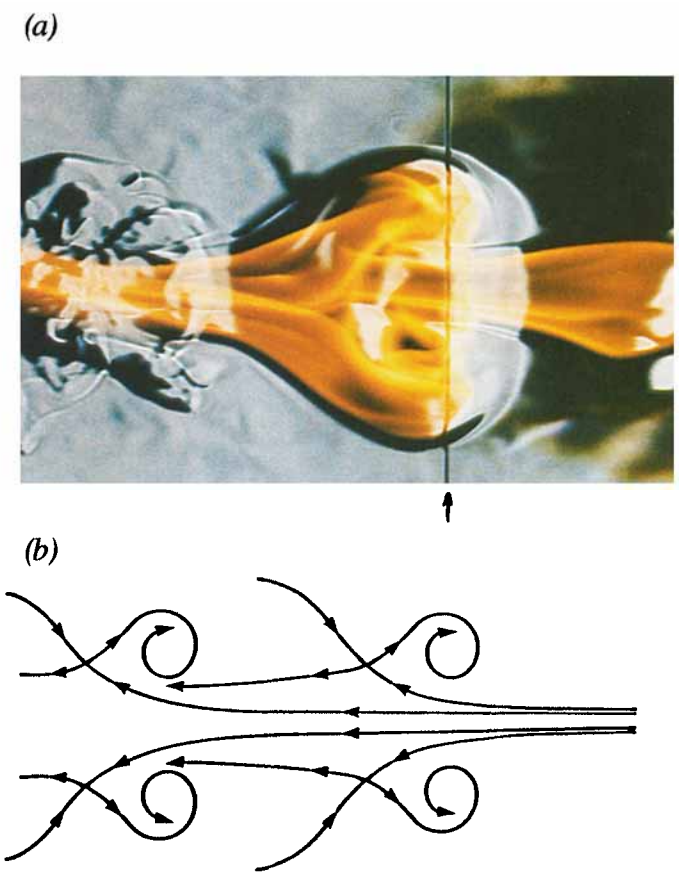

FIGURE 16. As figure 15 but for the weakly coupled case.

frequency range in the forced flow, a double structure is observed with two distinct wavelengths: a long wavelength associated with the luminous buoyancy-driven core flow, and a short wavelength associated with the shear-driven outer flow which is identified with the envelope of the schlieren image.

For all pressures and velocity ratios examined, the character of the flow changed significantly at an excitation frequency close to the natural flickering frequency, and we have called this the strongly coupled state. This state was characterized by a pinching-off of the flame to form flamelets. The luminous flame and the schlieren image of the outer flow structure moved with a single overall wavelength. See figures 5(*a*), 6(*a*), and 7(*a*), and Strawa & Cantwell (1985). In addition, this state was characterized by an increase in the brightness of the flame and by a 20% reduction in the visually observed flame height. The acceleration of the flow on the axis of the jet also decreased significantly. The visual spreading angle measured from photographs of the flame was found to increase by about 25%. Although U_J for the 239 kPa case (figure 6) is about half that of the other two pressure cases, the structure and character of the flame is the same as the other cases. The strong coupling frequency was always at about 10 Hz and was not significantly affected by the initial jet exit or free-stream velocities as long as these remained in the buoyancy-dominated range.

Another periodic condition existed at an excitation frequency of about twice that associated with the strongly coupled condition. Here the flame ceased pinching-off and took on a character reminiscent of the unforced flame except that it was more regular and had a shorter wavelength coincident with the higher frequency forcing. We call this the weakly coupled state and it is typified by figures 5(*b*), 6(*b*), and 7(*b*). As the frequency of excitation was increased from the strong coupling frequency near 10 Hz to a range between 12 and 16 Hz, the flame exhibited a transitional mode that was characterized by a non-periodic switching between the strongly coupled and weakly coupled states. This switching occurred at intervals ranging from 1 to 5 s. Although in this paper we are mainly concerned with characterizing the strongly and weakly coupled cases, the flame behaviour in this chaotic intermediate state is of significant interest and is a subject of further investigation.

The natural frequency of the flame was measured using a stroboscopic lamp as the source for the schlieren system. The strobe frequency was manually varied until the schlieren image of the flame was held nearly stationary as viewed on a ground glass. The natural frequencies determined in this manner are listed in table 1. In all the cases studied the natural frequencies are about 10 Hz. When the flame was forced, the schlieren image could be frozen on the ground glass by driving the strobe light with the same frequency generator that drove the speaker. The visually observed flame heights and spreading angles and other overall properties of the flame behaviour are tabulated in table 1. Flame height, H, was determined by observing the height of the luminous zone and comparing with a ruler attached to the test section. Flame spreading angle, α, was determined from the visualization photographs. Flame heights were observed to decrease with increasing pressure owing primarily to more rapid mixing at the higher Reynolds number.

Dashed lines in figures 5, 6, and 7 trace the trajectory of a pronounced bulge in the luminous part of the flow. Solid lines trace the trajectory of a corresponding bulge in the outer flow. In sequence (*b*) of all three figures, the weakly coupled case, the acceleration of the inner flow is seen clearly as the luminous bulge passes through two outer-flow bulges before exiting at the top edge of the picture. The outer-flow bulges propagate downstream at a constant velocity; hence, the solid line is straight

whereas the inner-core, dashed line curves upward, indicating a strong acceleration. In sequence (*a*), both the solid and dashed lines are straight and have the same slope, indicating that the inner and outer flows are moving together. The phase velocity at which the flamelet moved downstream, U_{PH}, was determined from the slopes of the solid lines, and is given in table 1.

The flame also exhibits a wide variation in the brightness of the core flow in both space and time. Part of this variation is related to the fact that the depth of field is of the order of the overall width of the flame, and therefore the film exposure is proportional to the depth of the radiating material as well as its intensity. This effect is responsible for the fact that the centre of the flame is dark while the edges are bright; one is looking through a roughly axisymmetric luminous sheet. However, some of the variations in brightness appear to be due to real effects. This variation becomes even more obvious when the motion pictures of the flame are viewed. The effect is particularly noticeable in figure 5(*a*) where the evolution in brightness is indicated by a pointer. By the third and fourth figures from the left, the outer region of the flame is glowing more brightly and the colour has changed from orange to white. The pictures suggest a significant increase in temperature, possibly caused by oxygenation associated with increased entrainment and diffusion of free-stream air. It is also possible that the increased brightness is due to an increase in the size or number density of soot particles; however, one would not expect this to modify the colour of the flame. Karagozian & Manda (1986) analytically studied the distortion of a two-dimensional fuel strip due to the interaction with a vortex pair. The vortex pair was counter-rotating and placed at the fuel-oxidizer boundary. Their analysis shows a laminar flame roll-up somewhat similar to that observed in figure 5(*a*).

Yule *et al.* (1980) and Roquemore *et al.* (1984) have observed a more complex flow structure at higher jet speeds, with an additional instability in the initial jet region that influenced the inner structure of the flame. In our experiments, however, the flow does not exhibit this additional inner-jet instability. We feel that this is because the jet exit velocity in the present study was smaller than in the previous studies and buoyancy dominates throughout the flow. Owing to the lower velocity, the temperature profile across the jet quickly flattens out and buoyant forces accelerate the core fluid nearly uniformly. Thus the shear layer that caused the inner structure observed at higher flow speeds was not established here.

Inspection of the photographs at various pressures shows that as the pressure, and consequently the Reynolds number is increased, more small-scale structure appears in the flow. Moreover, the flame becomes more compact as the pressure is increased, which is consistent with the experiments of Flower & Bowman (1985) and McArragher & Tan (1972).

In the strongly coupled case, as the Reynolds number is increased the flow continues to be very periodic, even to the extent that much of the three-dimensional structure of the flame is repeated from cycle to cycle. The reader is invited to examine some of the details in the sequence of pictures shown in figure 7(*a*). Notice that in the first, third, and fifth frames the flow is approximately at the same phase, and one can compare the detailed flow structure of three successive eddies. Details of the luminous flame are repeated to a surprising degree. Similar repeatability of the fine-scale structure was observed by Subbarao (1987) in a helium coflowing jet at $Ri = 1.6$. On the other hand, in the weakly coupled case shown in figure 7(*b*), the flame is very broken up and does not exhibit the same repeatability. In both cases the large-scale structure of the flow is periodic and, except for the onset of small scales, looks essentially the same at all three pressures.

It was stated in §3 that the flame was insensitive to the initial conditions and, in terms of its overall behaviour, this is true. But the details of the flow seen so repeatably in figure 7(*a*) must in some sense reflect details of the initial conditions which are obscured when the forcing is at the higher frequency. Crudely speaking, under strongly coupled conditions, the large eddies convect away from one another so that mutual interactions, such as pairing, do not occur. This allows the small scales to develop with minimal straining by the large eddies. The small scales may thus retain their identity and early history for a considerable length of time.

But this does not explain the sensitivity to excitation frequency. For the same overall heat release rate, as determined by the flow rate, the excitation controls the detailed distribution of near-field mixing and heat release. This determines the initial temporal and spatial distribution of light fluid that is acted upon by buoyancy which, in turn, determines the downstream flow field. The essential conditions needed to realize strong coupling are positive buoyancy in the presence of coflow and excitation near the natural oscillatory frequency of the flame. The limitations of the present experiment prevent us from considering this issue further except to note the need for investigation of the near field in order to clarify the relationship between initial heat release and flow excitation.

6.2. *Velocity measurements*

Generally speaking, the velocity data support the visual observations. In the strongly coupled state, there is a reduction in centreline average velocity by up to 50%, while centreline r.m.s. velocity fluctuations in the entrained free-stream fluid are reduced by 30%, and in the jet fluid are reduced by 50% (see figures 8, 9, 10, and 11). The error bar in figure 8 indicates our best estimate of the velocity measurement uncertainty resulting from effects of thermophoresis, sampling bias and instrument error.

One can think of the velocity in this flow as being composed of three parts: an overall average, $\langle u \rangle$; a periodic component, u_ϕ; and a random fluctuation, u'; or

$$u = \langle u \rangle + u_\phi + u'. \tag{11}$$

The traditional overall r.m.s. velocity is $u_\phi + u'$. By conditioning the velocity data with respect to the excitation signal, the periodic component of the velocity can be determined. Overall average, $\langle u \rangle$, and r.m.s., $(u'^2)^{\frac{1}{2}}$, velocity profiles for the 446 kPa case are plotted in figures 8 and 9. Figure 8 is the profile with water seeding only, and figure 9 is the profile with Al_2O_3 seeding only. In figures 8 and 9, the periodic component of the velocity has been separated out so that the r.m.s. fluctuations are a measure of the random part of the turbulence flux.

Figure 8 shows that, for all cases, water droplets reach the flow centreline, indicating that cold free-stream fluid has been entrained to the centreline. Comparing figures 8 and 9, we see that the water profiles are symmetric while the Al_2O_3 profiles are less symmetric. Both water and Al_2O_3 profiles show that the average centreline velocity in the strongly coupled case (represented by circles) is about half that of the weakly coupled case (represented by diamonds) and is somewhat less than the velocity in the unexcited case. Water seeding indicates an average velocity profile that is more full and more evenly distributed under the strong coupling condition. Additionally, r.m.s. velocities are substantially reduced in the strongly coupled case. The Al_2O_3 data show a reduction in turbulence level; the ratio of r.m.s. velocity to average velocity drops from 0.2 in the weakly coupled case to 0.05 in the strongly coupled case. This reduction in turbulence level is consistent with the enhanced

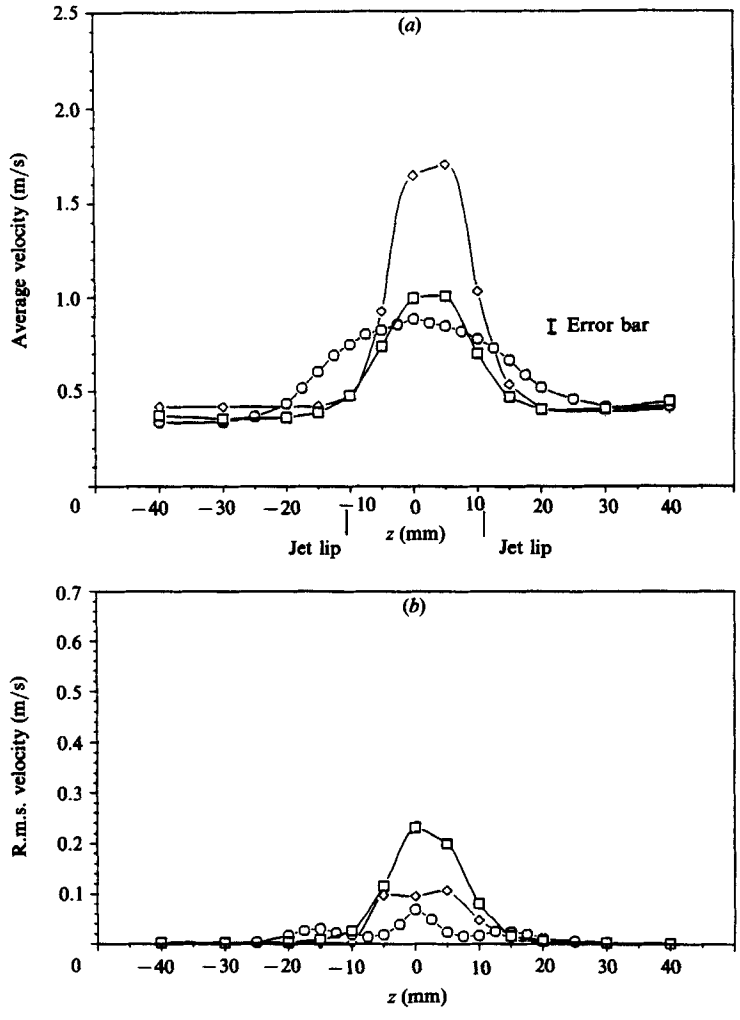

FIGURE 8. Overall LDA velocity plot for 446 kPa with water seeding, cases 7A, 8A, and 9A. (*a*) Velocity averaged over all phase bins, $\langle u \rangle$; (*b*) r.m.s. velocity after the periodic component has been subtracted out, u'. The location of the jet-tube wall and an error bar are shown. The measurements in figures 8–14 were taken 3 jet diameters from the jet exit. □, Unexcited; ○, low frequency; ◇, high frequency.

organization observed in the visual images of figure 7(*a*). The broadened profiles and the faster burnout rate suggest better mixing in the strongly coupled case in spite of the reduced turbulence level.

Figures 10 and 11 are phase-conditioned velocity profiles of measurements made at the centreline of the flow for both types of seeding at 446 kPa. During data reduction, the excitation period is divided into 30 phase bins. Each data point is allocated to one of these bins. The abscissa for all the centreline plots is the phase-bin number. Each centreline profile consists of two plots. In the upper plot, the number of data points collected for each bin relative to the total number of data points collected for all the bins is plotted versus phase bin. Average and r.m.s. velocities are calculated for each phase and plotted in the lower plot. Figures 10(*a*) and 10(*b*) are centreline profiles with water seeding at 446 kPa for strong and weak

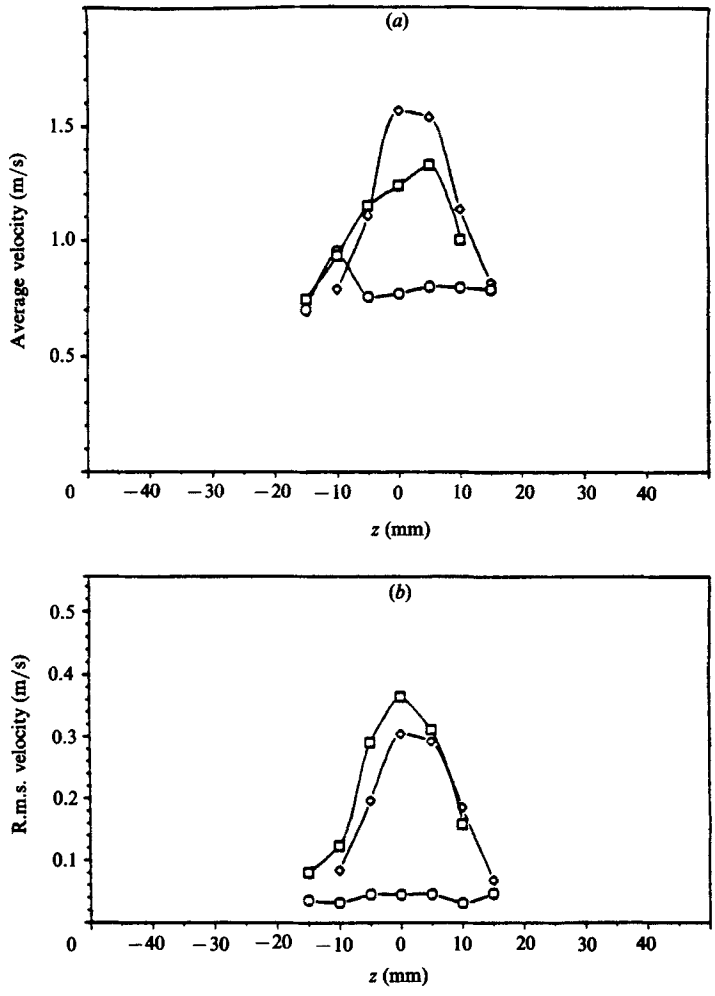

FIGURE 9. Overall LDA velocity plot for 446 kPa with Al_2O_3 seeding, cases 7B, 8B, and 9B. (*a*) Velocity averaged over all phase bins, $\langle u \rangle$; (*b*) r.m.s. velocity after the periodic component has been subtracted out, u'. Legend as for figure 8.

coupling (see cases 8A and 9A in table 2). Figures 11 (*a*) and (*b*) are centreline profiles with Al_2O_3 seeding at 446 kPa for strong and weak coupling (see cases 8B and 9B in table 2).

In figure 10 (*a*, *b*) we see localization of seed particles relative to phase, and a periodic variation in bin average and r.m.s. velocity. Water droplets fail to reach the centreline during roughly 20% of the cycle. A comparison of the upper graphs of figure 11 (*a*, *b*) reveals that the distribution of Al_2O_3 is nearly uniform with phase for the weakly coupled case (9B), but it is strongly localized with phase for the strongly coupled case (8B). This is a clear indication that in the strongly coupled case the jet fluid pinches off, forming pockets of fuel separated by regions of entrained air. In the weakly coupled case the jet fluid shows relatively little periodic variation. Both features of the phase-averaged velocity data are consistent with figures 6 and 7, which show that the luminous part of the flame is periodic in the strongly coupled case and is randomly broken up in the weakly coupled case. Data rates on the

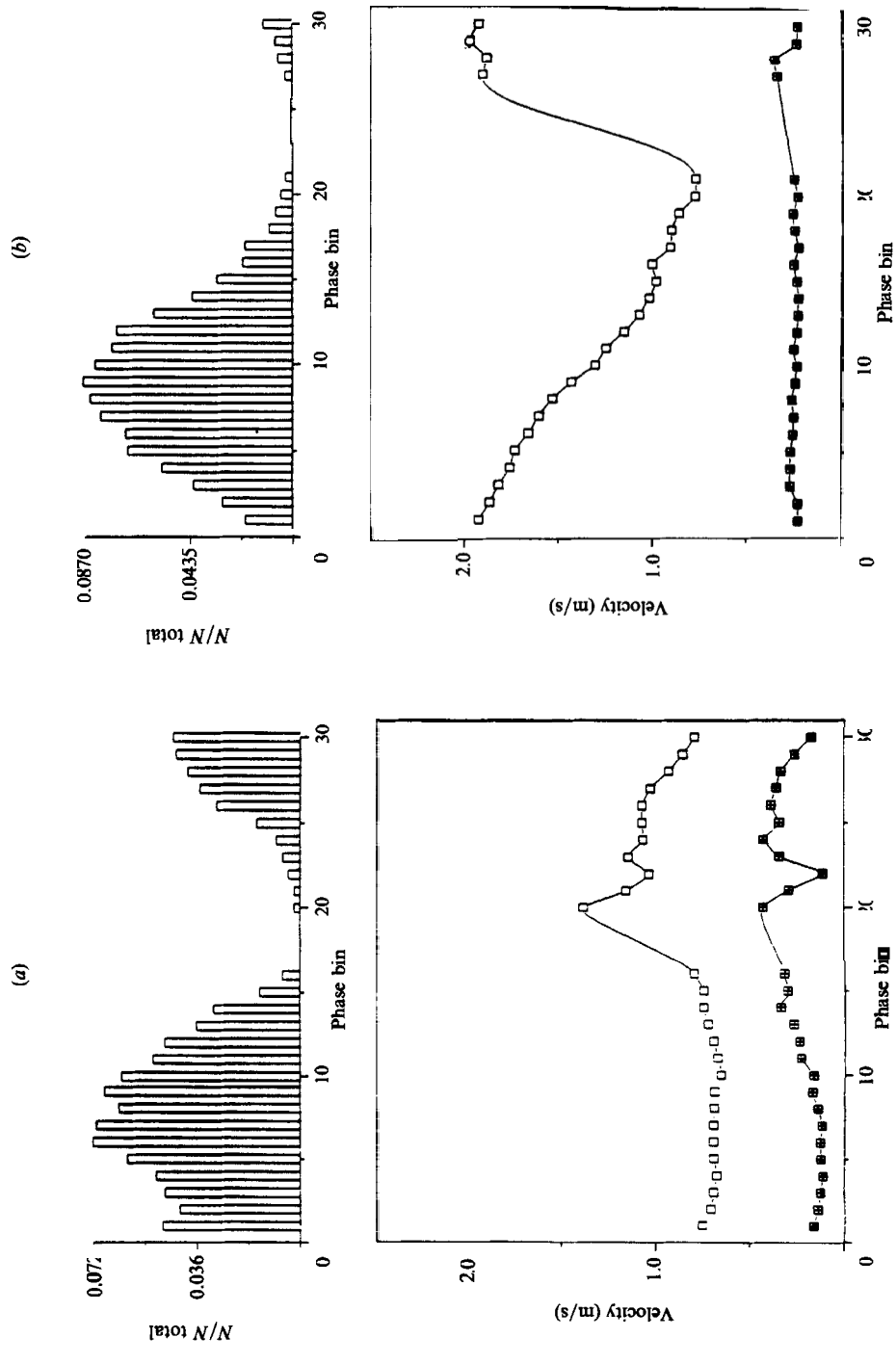

FIGURE 10. Graphs of phase-conditioned data taken on the flow centreline at 446 kPa with water seeding: (*a*) excitation frequency is 9.6 Hz, case 8A; (*b*) excitation frequency is 20 Hz, case 9A. The upper plot shows the variation in data population as a function of phase while the lower plot shows the bin average (□) and r.m.s.-velocity variation (⊞) as a function of phase.

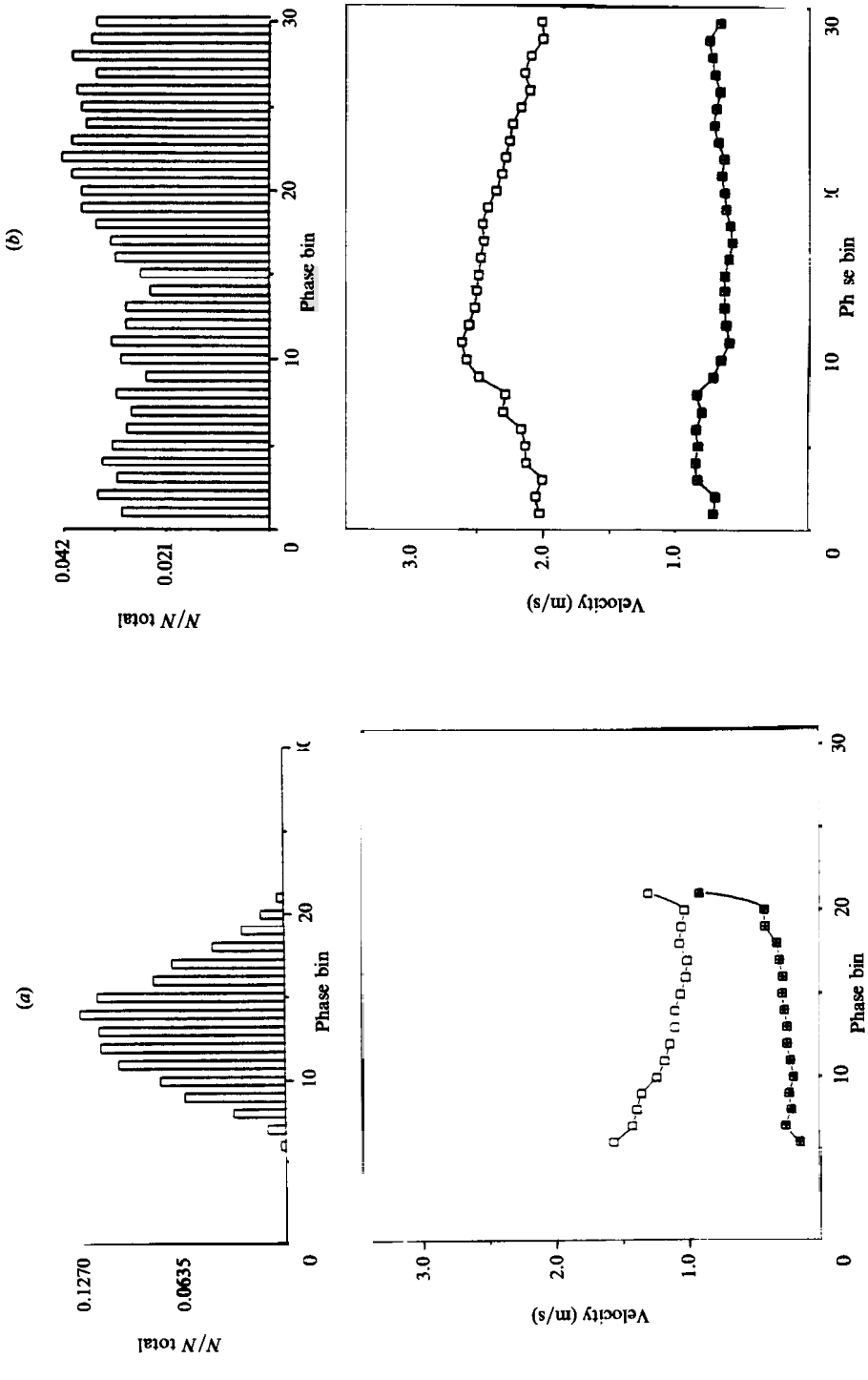

FIGURE 11. Graphs of phase-conditioned data taken on the flow centreline at 446 kPa with Al_2O_3 seeding: (*a*) excitation frequency is 9.6 Hz, case 8B; (*b*) excitation frequency is 20 Hz, case 9B. The upper plot shows the variation in data population as a function of phase while the lower plot shows bin average (□) and r.m.s.-velocity variation (⊞) as a function of phase.

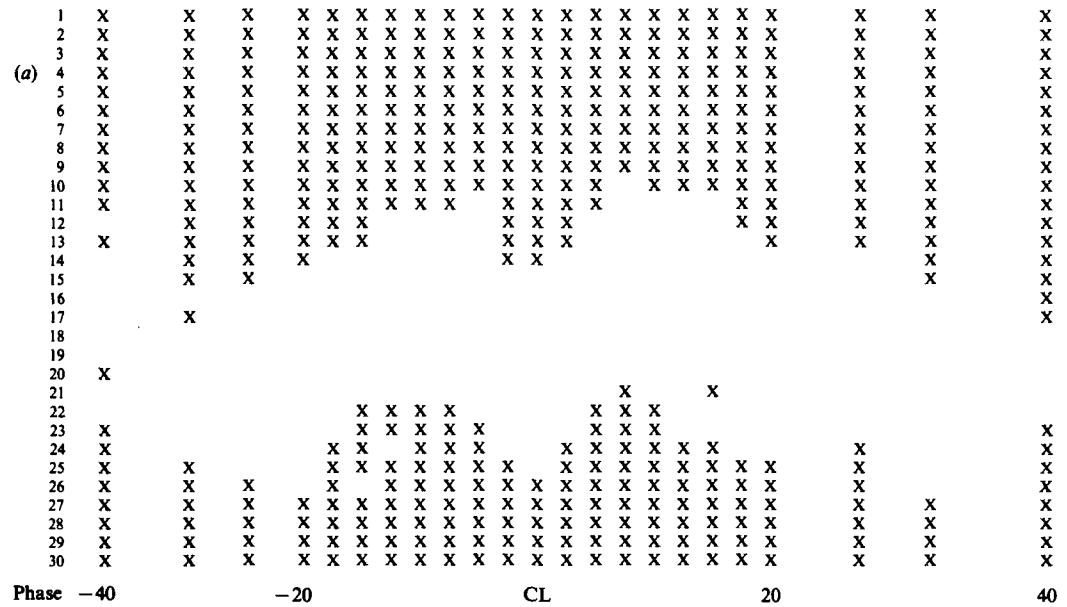

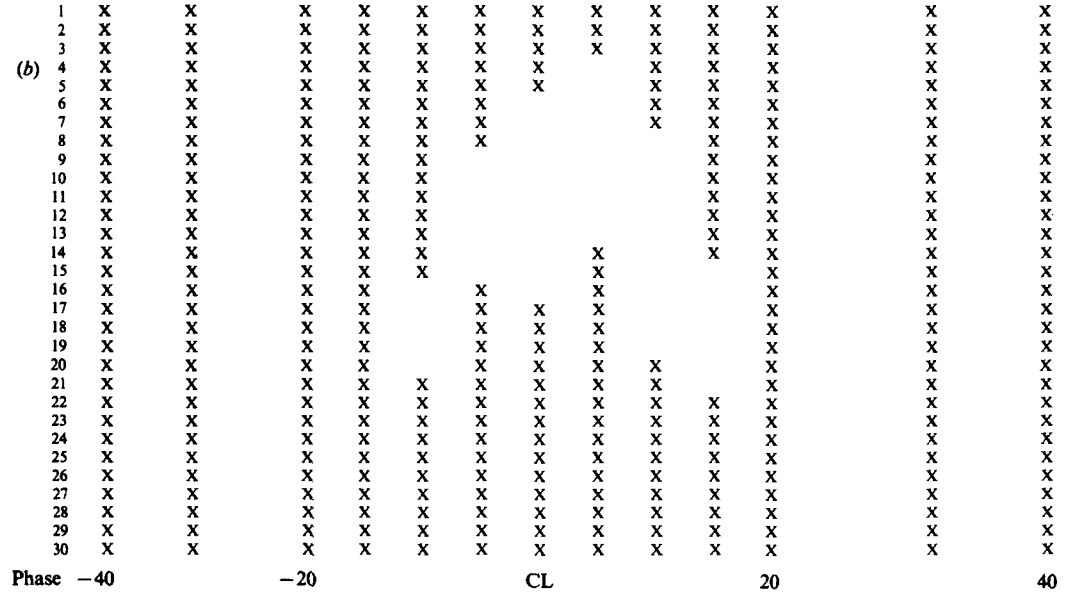

FIGURE 12. Threshold portraits of population-density data at 446 kPa with water seeding: (*a*) excitation frequency is 9.6 Hz, case 8A; (*b*) excitation frequency is 20 Hz, case 9A. An 'X' is printed when the density is greater than the threshold value. The threshold value in (*a*) is 2% of total points collected at a location, while (*b*) is 1%.

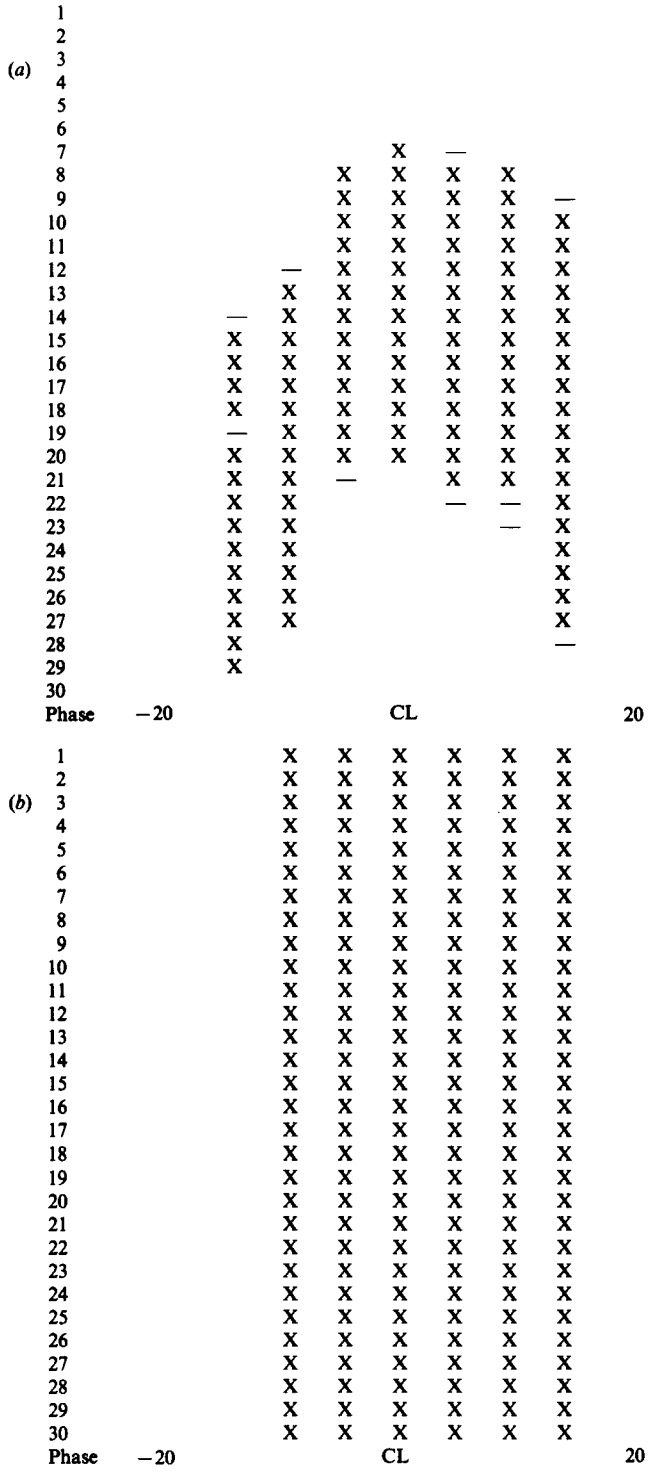

FIGURE 13. Threshold portraits of population-density data at 446 kPa with Al_2O_3 seeding: (*a*) excitation frequency is 9.6 Hz, case 8A; (*b*) excitation frequency is 20 Hz, case 9A. An 'X' is printed when the density is greater than the threshold value. The threshold value in both cases is 1%.

centreline for Al_2O_3 in the weakly coupled case at all pressures were an order of magnitude greater than for the strongly coupled case, indicating less dispersion of particles away from the centreline in the weakly coupled case.

In order to more clearly define the flow-field structure, it was useful to visualize where the cold free-stream fluid and jet fluid existed in the flow. This was done using population data of the type shown in the upper plots of figures 10 and 11. Based on estimates of the evaporation rates of the water droplets produced by the atomizer, it was assumed that the droplets quickly evaporated as they approached the hot reaction zone and thus roughly mark the location of the cold free-stream fluid. The Al_2O_3 particles roughly mark the location of the jet fluid.

Figures 12 and 13 are threshold portraits of population density at 446 kPa with water seeding and Al_2O_3 seeding, respectively. In order to construct these figures, it was necessary to use a criterion for choosing a threshold. This was done as follows. With Al_2O_3 seeding only, large data densities are expected when fluid originating in the jet passes the measurement station and low data densities are expected when fluid originating in the free stream passes the measurement station. In the case of water seeding, the peak at high densities corresponds to cold free-stream fluid, while the peak at low densities corresponds to fuel and combustion products. In the case of Al_2O_3 seeding, the peak at high densities corresponds to jet fluid, while the peak at low densities corresponds to free-stream fluid. In both cases a histogram is made of the data densities that occur at each phase. This histogram has a bimodal structure with one peak at low data densities and one at high densities. A threshold is picked between the peaks and a picture is produced with an 'X' appearing at a location where the density is above the threshold, and a blank appearing if the density is below the threshold. This is called a threshold portrait and the technique is more fully explained in Strawa (1986). The threshold used for case 8A was 2% of the total population at a given location, while the threshold used for the other cases was 1%.

Figure 12 shows portraits for cases 8A and 9A with water seeding. The X in these figures correspond to cold free-stream fluid (high data densities) while the 'hole' corresponds to hot combustion products. Comparing figures 12(*a*) and 12(*b*), we see that the reaction process is confined to a much smaller area in the weakly coupled case than in the strongly coupled case. The hole for the weakly coupled case is narrow, not exceeding $z = \pm 15$ mm in the spanwise direction, and long, extending about 20 phase bins. In contrast, the structure in the strongly coupled case is wide ($z = \pm 25$ mm) and short, in agreement with the photographs. One of the distinctive features of figure 12(*a*) is the dimple indicating relatively cold fluid at the top of the eddy and the associated hot tail at the bottom of the eddy on the centreline. Both of these features can be picked out in figure 7(*a*). They seem to be connected to the existence of saddle points in the flow, and they will be discussed in the next section. Figure 13 shows portraits for cases 8B and 9B with Al_2O_3 seeding. The X in these figures correspond to jet fluid. Here the pinching-off of the fuel to form flamelets under strong coupling is particularly noticeable; under weak coupling, the fuel extends all along the centreline at all phases.

7. Flow topology

In the following discussion the velocity measurements and visual data are combined in an attempt to construct a topological picture of the flow. Topological methods have been used successfully in the description of unsteady flow patterns in

cold flows and a review of the subject is given by Perry & Chong (1987). The approach is useful because it provides an unambiguous language for describing flow structure. In addition considerations of the topological constraints on a flow can often be used to sketch a complete flow pattern from a minimum amount of data. The ability to sketch flows often leads to new knowledge. In recent years we have seen a significant increase in our understanding of three-dimensional separated flows due largely to the application of topological methods to this problem.

Perry & Chong discuss the use of critical-point theory to describe unsteady flow patterns in free shear flows. In a frame of reference moving with the flow, the velocity field is seen as a moving pattern of critical points whose topology is related to the local vorticity, pressure and strain at the point. Regions where the strain rate is large compared with the vorticity appear as saddle points. In the context of flame studies regions of high strain are significant in that they are associated with flame extinction. Flame topologies are likely to be more complex than in cold flow owing to the volume changes associated with heat release and the dependence of local trajectories on the temperature field. In this paper we attempt to extend the use of topological methods to the description of flames in the hope that we may better understand the interaction between the unsteady flow field and the combustion process.

Maps of the unsteady, streamwise velocity field have been constructed for the low- and high-frequency cases from the 446 kPa data. These are displayed in figure 14. The shaded regions in these figures correspond to the holes in figure 12. Since only streamwise velocity measurements were made, information concerning the velocity vector field is incomplete. However, a qualitative knowledge of the entrainment and large-scale transport processes that affect the flame can be obtained by considering the streamwise velocity data together with the flow-visualization pictures.

The velocity field shown in figure 14 is viewed from a reference frame moving with the large-scale eddies in the flow. The spanwise location is labelled across the bottom of the map. In order to more easily relate the measured velocity to visualization of the flame, phase increases from top to bottom on the figure. One can think of a structure moving past a stationary probe. The top of the structure will pass the probe during early phases, and the tail of the structure will pass at later phases. Displaying figure 14 in this way shows the top of the structures at the top of the page just as a photograph would display them. The data may roughly be equated to a picture of the flow transforming the time-like phase coordinate to a spatial coordinate. Following Favre, Gaviglio & Dumas (1967) we shall use the term 'celerity' to refer to the velocity of propagation of the large eddies in the flame. The celerity used in figure 14 was taken to be 0.72 m/s, corresponding to the phase velocity derived from the slope of the solid line in figure 7(*a*). Selection of the celerity is somewhat arbitrary, but the resulting flow characteristics should be relatively insensitive to small changes in celerity. The flow fields of figure 14 did not change appreciably for changes in the celerity of 10%.

The velocity fields in figure 14 are combined with the visual data of figure 7 to form the sketches in figures 15 and 16 (plate 4), which represent kinematic descriptions of the strongly and weakly coupled cases. The sketches are placed alongside photographs of the luminous and schlieren image of the flame. The sketches describe the overall mean motion of the unsteady field, and not the small, turbulent motions that are also visible in the photographs. When comparing velocity data with the photographs, it should be remembered that a photograph is an x versus y representation of the flow at one instant in time, whereas the velocity data comprise an x versus time representation of the flow taken at one y-location. As a result, the

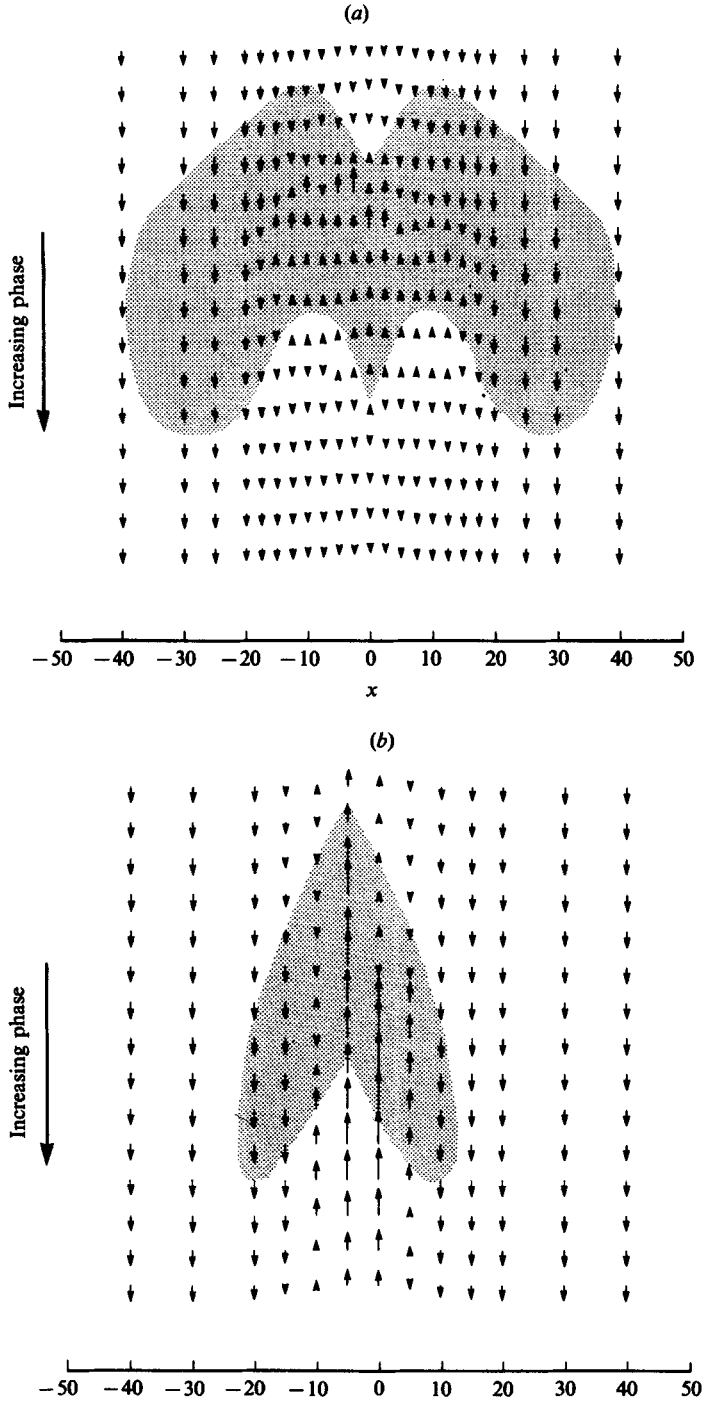

FIGURE 14. Maps of the unsteady, streamwise, velocity field for 446 kPa with water seeding at: (*a*) the strongly coupled condition, and (*b*) the weakly coupled condition. The abscissa in both maps is the spanwise dimension while the ordinate is phase, increasing down the page. A celerity of 0.72 m/s has been subtracted out so the vectors are in the reference frame moving with the large eddies. The shaded areas match the 'holes' observed in the threshold portraits of figure 12.

velocity data are a distorted version of a photograph in that faster parts of the flow are compressed into a small number of phases and slower parts of the flow are stretched over many phases. The arrow in the frames indicates the location at which the velocity measurements were made.

The vector field in figure 14(*a*) indicates the presence of stagnation points on the flow centreline above and below the region of hot combustion gases. Two stagnation points are also suggested by the vector field in figure 14(*b*), however, these appear to be located on either side of the centreline near the upper end of the hot region. The contrast between the vector fields in figures 14(*a*) and 14(*b*) are evidence of the change in the structure of the flow field which occurs when the flame is excited near its natural frequency. In figures 15 and 16 the flow fields are sketched as consisting of a series of saddles and foci. These features are inferred from the flow patterns in figure 14 as well as from the threshold plots and still photographs. The rotation sense of the eddies is inferred from visual evidence in the high-speed movies. The eddies are shown as stable (spiralling in) foci rather than as closed centres or as unstable foci (spiralling out). This is the most conjectural aspect of the sketches. The presence of heat release and regions of rapid heating and cooling preclude the vortices from being drawn as closed centres. However, there is no hard information to determine whether the trajectories spiral in or out. The sense of rotation is no guide in this. The issue hinges on precisely locating the critical points and evaluating the divergence of the local flow field at the point. If there is local heating corresponding to a volume source, the trajectories will spiral out perhaps toward a limit cycle formed with entrained fluid spiralling in. If the temperature at the critical point is decreasing, corresponding to a local volume sink then trajectories will spiral in. In figures 15 and 16 we have tacitly assumed that the fluid near the focus is cooling as it rolls up, which is consistent with the assumption that the eddy as a whole will cool as it rises, although this cannot be assured until the fuel is completely burned out.

The topology of figure 15(*b*) indicates a direct saddle-to-saddle connection by a single separatrix which, strictly speaking, is structurally unstable except under conditions of strong symmetry (Chapman 1986). There are alternative, structurally stable descriptions of this flow in which there are no saddle-to-saddle connections but, instead, the separatrices are infinitesimally close to one another. The resolution of our measurements was such that we could not distinguish between the structurally stable and unstable patterns. For simplicity we have used the topology shown in figure 15(*b*).

Perry, Lim & Chong (1980) used critical-point theory to describe the flow structure found in an excited neutrally buoyant jet (e.g. see their figure 8*b*). It is interesting to note that the topology of the flame seen in figure 15(*b*) is very similar to the topology that they observed in the excited jet, providing support for the idea of constructing complex flow fields from a limited set of critical-point flow patterns.

In any case, it appears that when the flame is forced near its natural frequency, instability modes couple in such a fashion that the stagnation points, which are normally off the centreline of the flow, are caused to move to the centreline and merge. When this happens there is increased entrainment of cold free-stream air to the centreline, and more rapid mixing, causing the flame to pinch off, leading, in turn, to more rapid burnout. The distribution of LDA seed particles is consistent with this picture. Figure 17(*a–c*) represents one possible set of sketches which depicit the kinematics of the pinch-off process. For simplicity it is assumed that the flow remains axisymmetric throughout the transformation.

In figure 15(*b*) the upstream saddle is associated with the cold dimple referred to

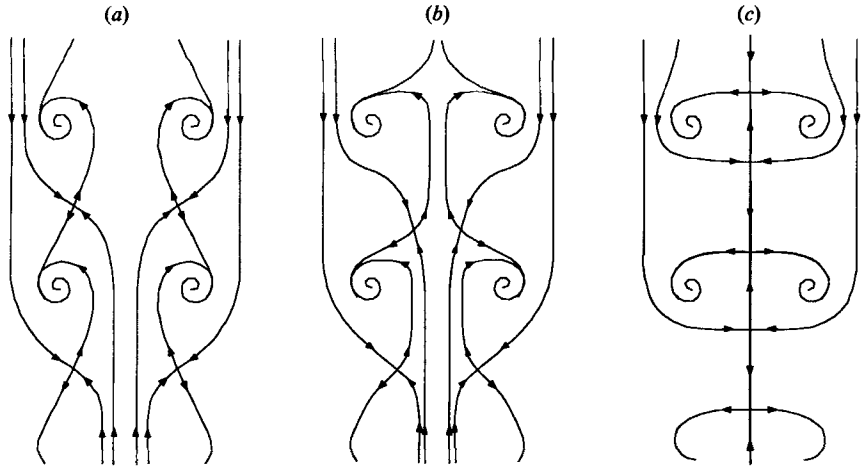

FIGURE 17. A sequence of sketches showing the possible evolution of flow topology and kinematics of flame breakup under weak (*a*) and strong (*c*) coupling conditions.

at the end of the previous section (see figure 14*a*). It carries cold entrained air away from the centreline into the hot eddies. The downstream saddle is associated with the hot tail of the eddy and brings free-stream air toward the centreline where it meets the relatively hot wake of the eddy. Part of this air helps to oxygenate the eddy upstream of the saddle, and part is carried downstream where it meets the top of the following eddy in the viscinity of the cold dimple.

8. Concluding remarks

This work was motivated by a desire to control flames and to better understand the relationship between unsteady flow structure and the combustion process. The geometry chosen for study is representative of a broad class of low-speed unpremixed flames subject to a classical flickering instability. The effect of axial forcing and increasing pressure on the structure and controllability of the flame has been studied in an attempt to elucidate some of the underlying mechanisms of flame control. The main effect of increasing pressure (or Reynolds number) is to cause a moderate decrease in the visual flame height and to produce small-scale motions through decreased relative diffusion. The large-scale structure and response to excitation remains more or less unchanged. The effect of axial excitation is to produce a controllable periodic flow providing a useful subject for detailed study. The flame is very sensitive to the frequency of the excitation, far more sensitive than the comparable cold jet but not particularly sensitive to the level of the applied perturbations as long as the amplitude does not fall below some minimum value, on the order of several percent of the jet exit velocity. Many different flame configurations are possible over a continuous range of excitation frequencies and we have focused on two cases which illustrate typical behaviour. When the flame is forced at a frequency close to the natural flickering frequency, the flame breaks up into a series of distinct eddies with a fine structure that is highly repeatable from cycle to cycle. It is conjectured that the flame breakup process is triggered by changes induced in the spatial and temporal distribution of buoyancy released in the flame sheet near the jet exit. An attempt has been made to use a combination of visual and velocity data to describe the kinematics of flame breakup in terms of

changes in flow topology seen in a frame of reference moving with the eddies. The topology of the flame is similar to the topology observed in cold jets suggesting that a limited set of critical-point flow patterns can be used as a common basis for the description of complex reacting as well as non-reacting flow fields.

This work was supported by the Air Force Office of Scientific Research under grant number 84-0373 and by the National Science Foundation under grant number 11869.

REFERENCES

BALLANTYNE, A. & BRAY, K. N. C. 1977 Investigations into the structure of jet diffusion flames. *Sixteenth Symp. (Intl) on Combustion*, pp. 777–787. The Combustion Institute.

BEKER, H. A. & LIANG, D. 1983 Soot emission, thermal radiation, and laminar instabilities of acetylene diffusion flames. *Combust. Flame* **52**, 247–256.

CHAMBERLIN, D. S. & ROSE, A. 1928 The flicker of luminous flames. *Indust. Engng Chem.* **20**, 1013–1016.

CHAPMAN, G. T. 1986 Topological classification of flow separation on three-dimensional bodies. *AIAA paper* 86-0485.

CHIGIER, N. A. & YULE, A. J. 1979 The physical structure of turbulent flames. *AIAA paper* 79-0217, pp. 1–8.

DIBBLE, R. W., KOLLMANN, W. & SCHEFER, R. W. 1984 Measurements and predictions of scalar dissipation in turbulent jet flames. *Twentieth Symp. (Intl) on Combustion*, pp. 345–352. The Combustion Institute, Ann Arbor, Mich.

FAVRE, A., GAVIGLIO, J. & DUMAS, R. 1967 Structure of velocity space–time correlations in a boundary layer. *Phys. Fluids* **10**, S138–S145.

FLOWER, W. L. & BOWMAN, C. T. 1985 *Twentieth Symp. (Intl) on Combustion*, pp. 1035–1044. The Combustion Institute. Ann Arbor, Mich.

FRIEDLANDER, S. K. 1977 *Smoke, Dust and Haze*. Wiley.

GRANT, A. J. & JONES, J. M. 1975 Low frequency diffusion flame osscilations. *Combust. Flame* **25**, 153–160.

KARAGOZIAN, A. R. & MANDA, B. V. S. 1986 Flame structure and fuel consumption in the field of a vortex pair. *Combust. Sci. Tech.* **49**, 185–200.

LEPICOVSKY, J. 1986 Laser velocimeter measurements of large-scale structures in a tone-excited jet. *AIAA J.* 27–31.

LEWIS, G. S., CANTWELL, B. J. & LECUONA, A. 1987 The use of particle tracking to obtain planar velocity measurements in an unsteady laminar diffusion flame. *Paper 87-35, meeting of Western States Section/The Combustion Institute, Provo, Utah.*

LEWIS, G. S., CANTWELL, B. J., VANDSBURGER, U. & BOWMAN, C. T. 1988 An investigation of the interaction of a laminar non-premixed flame with an unsteady vortex. Paper accepted for the *Twenty Second (Intl) Symp. on Combustion*. The Combustion Institute, Pittsburgh.

MCARRAGHER, J. S. & TAN, K. J. 1972 Soot formation at high pressure: a literature review. *Combust. Sci. Tech.* **5**, 257–261.

PERRY, A. E. & CHONG, M. S. 1987 A description of eddying motions and flow patterns using critical-point concepts. *Ann. Rev. Fluid Mech.* **19**, 125–155.

PERRY, A. E. & LIM, T. T. 1978 Coherent structures in coflowing jets and wakes. *J. Fluid Mech.* **88**, 451–464.

PERRY, A. E., LIM, T. T. & CHONG, M. S. 1980 The instantaneous velocity fields of coherent structures in coflowing jets and wakes. *J. Fluid Mech.* **101**, 243–256.

RAYLEIGH, LORD. 1877 *The Theory of Sound*, vol. II, pp. 227–228. [Dover, New York, 1977.]

ROPER, F. G. 1977 The prediction of laminar jet diffusion flame sizes. Part 1. Theoretical model. *Combust. Flame* **29**, 219–226.

ROQUEMORE, W. M., TANKIN, R. S., CHIU, H. H. & LOTTES, S. A. 1984 In *ASME AMD – Vol. 66: Experimental Measurements and Techniques in Turbulent Reactive and Non-Reactive Flows* (Ed. R. M. C. So, J. H. Whitelaw & M. Lapp), pp. 159–175.

STRAWA, A. W. 1986 An experimental investigation of the structure of an acoustically excited diffusion flame. Ph.D. thesis, Stanford University. SUDAAR 558.

STRAWA, A. W. & CANTWELL, B. J. 1985 Visualization of the structure of a pulsed methane air diffusion flame. *Phys. Fluids* **28**, 2317–2320.

SUBBARAO, E. R. 1987 An experimental investigation of the effects of Reynolds number and Richardson number on the structure of a co-flowing buoyant jet. Ph.D. thesis, Stanford University. SUDAAR 563.

YULE, A. J., CHIGIER, N. A., RALPH, S., BOULDERSTONE, R. & VENTRURA, J. 1980 Combustion–transition interactions in a jet flame. *AIAA J.* **19**, 752–760.